




RESEARCH ARTICLE

Fundamental considerations in the design and performance assessment of propulsive fuselage aircraft concepts

N.G.M. Moirou , N.E. Mutangara  and D.S. Sanders 

Centre for Propulsion and Thermal Power Engineering, Cranfield University, Cranfield, Bedfordshire, UK

Corresponding author: Nicolas G.M. Moirou; Email: nicolas.g.moirou@cranfield.ac.uk

Received: 28 January 2024; **Revised:** 7 October 2024; **Accepted:** 10 October 2024

Keywords: boundary layer ingestion; computational fluid dynamics; performance accounting; propulsive fuselage concept

Abstract

Propulsive fuselage aircraft complement the two under-wing turbofans of current aircraft with an embedded propulsion system within the airframe to ingest the energy-rich fuselage boundary layer. The key design features of this embedding are examined and related to an aero-propulsive performance assessment undertaken in the absolute reference frame which is believed to best evaluate these effects with intuitive physics-based interpretations. First, this study completes previous investigations on the potential for energy recovery for different fuselage slenderness ratios to characterise the aerodynamics sensitivity to morphed fuselage-tail design changes and potential performance before integrating fully circumferential propulsors. Its installation design space is then explored with macro design parameters (position, size and operating conditions) where an optimum suggests up to 11% fuel savings during cruise and up to 16% when introducing compact nacelles and re-scaling of the under-wing turbofans. Overall, this work provides valuable insights for designers and aerodynamicists on the potential performance of their concepts to meet the environmental targets of future aircraft.

Nomenclature

b	local width parameter (m)
$\dot{\mathcal{E}}_k$	wake kinetic energy flux (J/s)
$\dot{\mathcal{E}}_m$	mechanical energy flux (J/s)
$\dot{\mathcal{E}}_p$	rate of pressure-defect work (J/s)
$\dot{\mathcal{E}}_\tau$	rate of viscous boundary work (J/s)
\mathcal{F}	force vector on a body (N)
FR	fineness ratio, = L/D (-)
\dot{h}	rate of change in altitude (m/s)
L	length (m)
L/D	length over diameter ratio (-)
\dot{m}	mass-flow rate (kg/s)
M_B	Mach number of the moving body (-)
\hat{n}	unit normal vector
\mathcal{P}_f	body force propulsor power (J/s)
\mathcal{P}_k	kinetic energy inflow rate (J/s)
\mathcal{P}_s	shaft power (J/s)
p	static pressure (Pa)
R, r	radius (m)
\mathcal{S}	control surface (m ²)
\mathcal{V}	control volume (m ³)

W	aircraft weight (N)
$\hat{x}, \hat{y}, \hat{z}$	cartesian coordinate system

Greek symbol

β_{boat}	fuselage boat angle ($^{\circ}$)
β_{plug}	fuselage plug angle ($^{\circ}$)
Δ	boundary layer area (m^2)
δ	boundary layer thickness (m)
Δ^*	boundary layer mass displacement area (m^2)
η_{trans}	transmission efficiency (%)
Θ	rate of volumetric pressure work (J/s)
Θ^*	boundary layer kinetic energy area (m^2)
ρ	density (kg/m^3)
$\bar{\tau}$	viscous stress tensor (Pa)
Φ	rate of volumetric viscous dissipation (J/s)
ψ_{slope}	fuselage slope angle ($^{\circ}$)

Sub-/Super-scripts

$()^*$	isentropic quantity
$()$	non-isentropic quantity
$()_{\infty}$	free-stream quantity
$()_{A/C}$	aircraft
$()_B$	quantity on body surface
$()_{BLI}$	boundary-layer ingesting propulsor
$()_e$	boundary-layer edge quantity
$()_{fus}$	fuselage
$()_P$	quantity on propulsor
$()_{PFC}$	propulsive fuselage concept
$()_{pod}$	podded turbofan
$()_{ref}$	reference fuselage/aircraft
$()_{rev,irr}$	reversible and irreversible quantities
$()_{TE}$	quantity at the trailing edge

1.0 Introduction

To realise the ambitious environmental goals set by the European Commission [1], it is notwithstanding that current aircraft are approaching their limit in terms of improvements in propulsive efficiency [2]. Therefore, in contrast to conventional configurations, there is an opportunity to exploit potential aerodynamic benefits with a closer integration between the airframe and propulsion system. Taking inspiration from the marine industry [3], a propulsor is integrated around the back of the airframe to ingest its boundary layer (BL) and achieve aero-propulsive performance improvements [2]. Whilst the kinetic energy excess imparted by the fuselage to the flow in conventional configurations is eventually wasted within the aircraft's wake, its ingestion by an aft-mounted thruster improves the aircraft performance by reducing its fuel consumption [4].

Amongst the conceptual aircraft based on boundary layer ingestion (BLI) reviewed by Moirou et al. [5], propulsive fuselage concepts (PFC) appear as the most pragmatic from their adaptation of conventional tube-and-wing aircraft, whereupon an aft-mounted propulsor encapsulates the tail-cone. Its direct installation on current airframes reduce the viscous dissipation that would otherwise have occurred in the wake by harvesting the energy present in the entire circumference of the fuselage's BL to produce a propulsive force. Additionally, the quasi-circumferential nature of the flow allows the flow-field to be approximated axi-symmetrically [6–8].

Whilst momentum-based approaches conventionally require the break-up of the airframe (drag) and propulsion system (force) to quantify thrust as a surrogate of the useful work generated by the propulsion system, challenges arise when high levels of integration are experienced, such as studied here. An alternative approach enables more physically intuitive interpretations and the quantification of the underlying physics, as well as circumventing potentially misleading associated metrics [4, 9, 10]. Assessing the different losses in the system from an absolute reference frame standpoint enables improved identification and interpretation of the causal mechanisms governing BLI aerodynamics. Unlike the relative reference frame that echoes experimental testing conditions, the absolute reference frame considers the aircraft as the moving body through an initially quiescent environment thus, imparting momentum and energy to its surroundings. The energy transferred to the flow can be traced to localised losses in different flow phenomena. This enables a decomposition, quantification and interpretation of the various mechanisms underlying BLI performance.

Aero-propulsive performance is inherently dependent on both the airframe and propulsion system. As such, it is important to assess the sensitivity of both with respect to changes in design and operating conditions. Ahuja and Mavris [11] explored the BLI performance sensitivities to airframe design changes with different nose shapes, 3D up-swept tails and tail ramps but with questionable metrics [12] and an emphasis on engines positioned like the MIT D8 [13] and ONERA NOVA [14]. Kenway and Kiris [15] investigated the wing downwash effects on the BLI fan inlet distortion and its importance in optimisation studies even though they pre-empt attenuated effects through simple wing-root re-designs. Despite the recommendations, wing-less airframes are of interest for reduced computational cost and focus on the impact of other design variables independently of the downwash generated. In that sense, Gray et al. [7] initiated a coupled aero-propulsive analysis with a single design variable (fan pressure ratio – FPR) at constant fan power input and concluded on the strong dependence of the overall performance to the aerodynamic and propulsive performance – also supported by Refs. [6, 8]. The coupling strength indicates that the overall aero-propulsive performance is likely to also depend on design variables such as the tail and nacelle geometries and fan input power. The knowledge gap in the flow behaviour when altering fuselage design parameters for integrating fully circumferential propulsors as found in propulsive fuselage concepts motivate the present study.

To address this gap observed, the present work first investigates the flow-field and its changes for various bare fuselage designs. The potential for energy recovery (PER) [4, 16, 17] and boundary layer parameters are compared for different fuselage nose shapes, and different conic and morphed tails in section, that will later accommodate the BLI propulsor. Then, the serpentine slope effects and its critical inclination angle are investigated. To bound the design space both axially and radially, the critical plug-cone angle is identified. These observations lead to multiple morphed tail designs from which PER is evaluated. The integration of aft-mounted propulsors at these different locations along the tail enables the coupled aero-propulsive performance evaluation developed by Moirou [12] to be applied in Section 3. In doing so, several propulsors are designed with different sizes and fan operating conditions and compared against a state-of-the-art short- to medium-range aircraft in Section 4. This work contributes toward the development and application of energy-based analyses on BLI aircraft, notably with the primary effects identified through this design space exploration. The recommendations may impact the airframe and engine manufacturers' decisions in their systems development to maximise fuel savings.

2.0 Fuselage design considerations

Taking a short- to medium-range (SMR) aircraft as reference, e.g. Airbus A321 of length 44.51m or Boeing B737-MAX10 of length 43.79m, the fuselage is isolated from its entire airframe. Its approximation and parametrisation given in Fig. 1 follow three distinct parts: an elliptic nose, a cylindrical cabin and a conic tail. All portions are driven by a fineness ratio, defined as the ratio of length over the radius of the component i ($FR_i = L_i/R_i$). In that respect, the ellipse follows as close as possible the aircraft's nose top-view, and the closest tail fineness ratio to the SMR aircraft's frustum tail, FR_{tail} , is derived with a boat-tail angle β_{boat} .

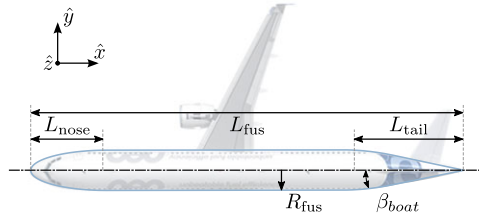


Figure 1. Schematic of the reference aircraft's bare fuselage approximation with an ellipsoidal nose and conic tail from an Airbus A321, from Ref. [12].

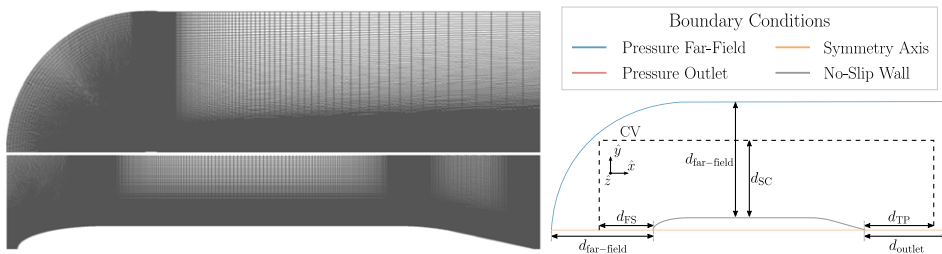


Figure 2. Grid of the bullet-shaped domain encapsulating the fuselage, grid close to the fuselage wall, and schematic of the domain, boundary conditions and analysis control volume.

The geometry modelling framework from Ref. [12] is used wherefrom the fuselage contour is extracted. Encapsulated within a bullet-shaped domain, the volume of the fluid is subsequently meshed following an automated structured grid generation routine using ANSYS ICEM 20.2 [18]. The bullet domain is defined such that its position does not interfere with the body through its boundary condition after undertaking a grid and domain size convergence study, based on the procedure from Celik et al. [19], and following Ref. [12]. As such, 10 fuselage chords are ensured upstream and around the fuselage ($d_{\text{far-field}}$), and 40 behind (d_{outlet}) as given in Fig. 2. The mesh follows a C-topology where elements close to the walls ensure a fineness with a y^+ falling between 0.9 and 1.0 along the entire body and coarsen the farther away. Representative flight conditions of an Airbus A321 are used for the CFD solved using ANSYS Fluent 20.2 [20] with a flight Mach number $M_B = 0.82$ at FL350 (35,000ft above sea-level) for $Re = 2.87 \times 10^8$. These conditions are set with a far-field pressure and a pressure outlet (Fig. 2). Turbulence is modelled using the two-equation Shear-Stress Transport (SST) $k - \omega$ model coupled with second-order spatial discretisation and the Green-Gauss cell-based gradient scheme. The fluid is considered as an ideal gas with piecewise-polynomial C_p variations, and the viscosity follows the temperature-dependent Sutherland's law. The specific heat ratio and thermal conductivity are kept constant and equal to 1.4 and 0.0242, respectively.

2.1 Nose-down selection considerations

An aircraft nose is often a distinguishable feature, and an isometric view suggests that no single profile can be extracted for a 2D axi-symmetric representation. To approximate its contour, top- and side views of an Airbus A321 are considered for reference and compared against three ellipsoidal approximations of different fineness ratios (Fig. 3). Distinctively, the closest approximation of the top and side views is given by an ellipse of $FR_{\text{nose}} = 3.71$ – semi-ellipsoid 2; and two noses of different fineness ratios are considered up to a hemispheric approximation, i.e. circular arc. The flow response to these different noses is investigated to help select the reference shape for future studies.

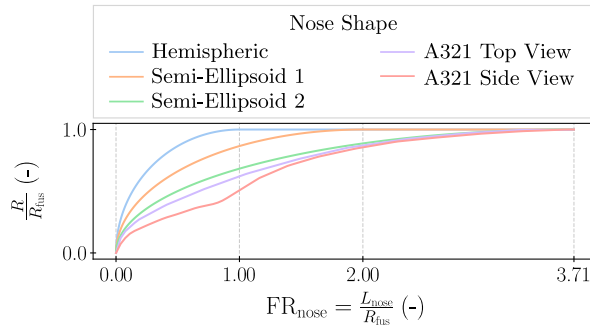


Figure 3. 2D axi-symmetric nose modelling of an A321 side- and top-view contours and elliptical approximations of different fineness ratios.

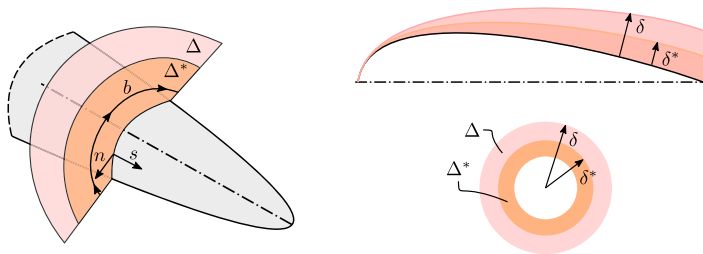


Figure 4. 2D and 3D axi-symmetric boundary layer parameters at cut planes around the fuselage tail, inspired from Ref. [16].

2.1.1 Figures of merit

To evaluate the differences in BL properties, the BL area Δ given in Equation (1a), its mass displacement area Δ^* , given in Equation (1b), and its kinetic energy area Θ^* in Equation (1c) are used. In comparison with the conventional 2D thickness definitions, these areas are applicable to 3D axi-symmetric scenarios whereby a local width parameter b is introduced [21] and illustrated in Fig. 4. This parameter relates the 2D and 3D definitions by considering the circumferential area at any radial position.

$$\Delta = \int_0^\delta b(n) \, dn \tag{1a}$$

$$\Delta^* = \int_0^\delta \left(1 - \frac{\rho V}{\rho_e V_e}\right) b(n) \, dn \tag{1b}$$

$$\Theta^* = \int_0^\delta \left(1 - \frac{V^2}{V_e^2}\right) \frac{\rho V}{\rho_e V_e} b(n) \, dn \tag{1c}$$

where δ quantifies the BL thickness in a 2D cut plane, ρ the fluid density and V its velocity and where e characterises the BL edge properties.

Along with the development of the BL properties, common mechanical energy-rate terms present in the energy- and exergy-based analyses [4, 9, 10] are calculated on survey planes along the fuselage. In doing so, the power balance is given in Equation (2) where the terms on the left represent the power sources to the flow with \mathcal{P}_s the amount of shaft power related to any moving fan’s blade, and \mathcal{P}_f the power input to the flow when the fan’s blades are substituted by a body force representation inside a volume. On the right-hand side, the sinks are represented by $W\dot{h}$ as the change in potential energy due to changes in altitude*, $\dot{\mathcal{E}}_m$ the mechanical energy deposition rate and Φ and Θ (Equations (3)) the system losses manifesting themselves under the form of viscous dissipation and volumetric pressure rates, respectively.

*This quantity is equal to the fuselage drag power, $\mathcal{F}_{fus} \cdot V_B$, when assuming steady-level flight

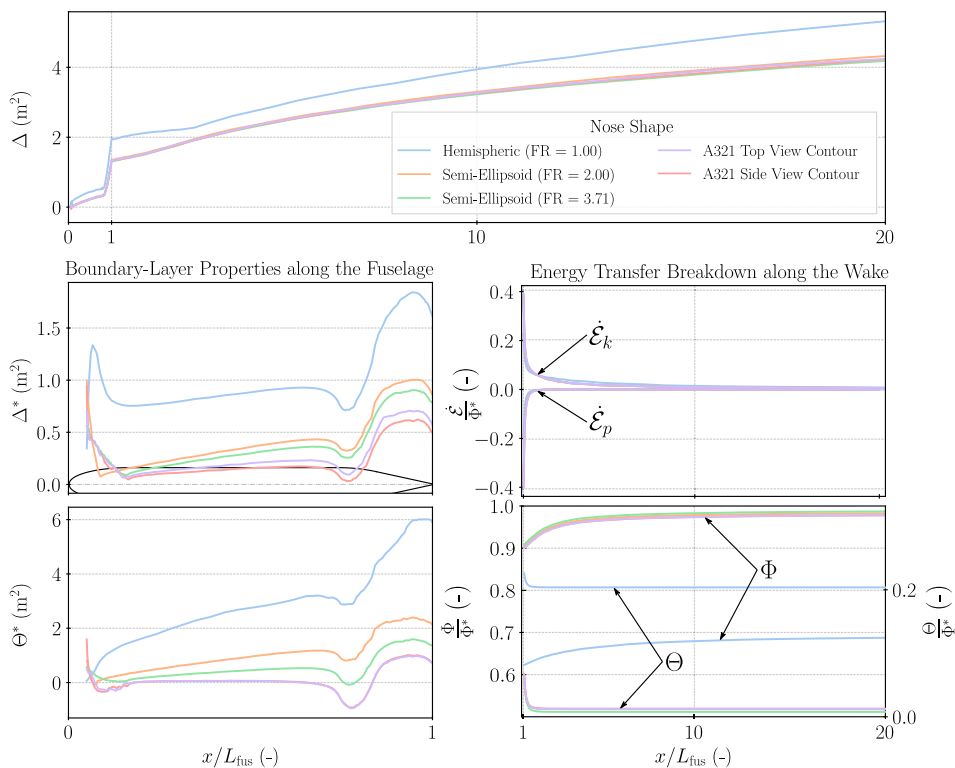


Figure 5. 3D axis-symmetric boundary-layer area (top), displacement area, momentum area and kinetic energy area (left) and wake energy-flux transfers and potential for energy recovery (right) for five different nose shapes at FL350 and $M_B = 0.82$.

$$\mathcal{P}_s + \mathcal{P}_t = Wh + \underbrace{\dot{\mathcal{E}}_k + \dot{\mathcal{E}}_p + \dot{\mathcal{E}}_\tau}_{\dot{\mathcal{E}}_m} + \Phi + \Theta \tag{2}$$

$$\Phi = \iiint_{\mathcal{V}} (\bar{\tau} \cdot \nabla) \mathbf{V} d\mathcal{V} \tag{3a}$$

$$\Theta = - \iiint_{\mathcal{V}} p_G \nabla \mathbf{V} d\mathcal{V} \tag{3b}$$

2.1.2 Flow response to nose shape

Figure 5 depicts the evolution of the BL area (Equation (1a)) both along the fuselage and within the wake, where it is observed that the hemispheric nose stands out from the other shapes. From the aircraft’s shoulder, a jump in the BL area caused by a strong local shock is noted. That shock is discernible from the mass displacement area Δ^* with a sharp increase that causes an unrecoverable thickening of the shear-layer. The semi-ellipsoid approximation of $FR_{nose} = 3.71$ stands amid the other shapes that are not subject to any shock. Its deviation from both A321 profiles yields a small difference in the BL properties but suggests a quasi-identical, yet greater, thickness and energy transfer from the fuselage to the flow. In other terms, a rear-mounted BLI propulsor will experience a slightly smaller mass-flow from the elliptic approximation than the more representative contours for a given propulsor size.

The difference in energy is confirmed by the right-hand side column’s charts that depict the flux transfer breakdown from the aircraft’s trailing edge to the Trefftz plane. The kinetic energy deposition rate $\dot{\mathcal{E}}_k$ and pressure-defect work $\dot{\mathcal{E}}_p$ are transferred into unrecoverable forms of energy Φ and Θ . The decay of power overtime results from the absence of a body that imparts additional energy to the flow,

which self-recovers to its initial quiescent form. Whereas a steep rate of dissipation is observed on the different nose shapes, the hemispheric nose necessitates more time to fully dissipate with a more gradual rate. Notably, the volumetric pressure work Θ cannot be neglected any longer as the shock left a residual irrecoverable pressure-defect work.

It is concluded that from the perspective of the BL growth, energy imparted to the flow and its recoverable part from an ideal device mounted at the aircraft's rear, the semi-ellipsoidal nose of $FR_{\text{nose}} = 3.71$ suits the nose shape approximation. However, it is stressed that the elliptic approximation is only acceptable under shock-free conditions which otherwise would dissipate a higher amount of non-recoverable energy and hence diminish the aerodynamic potential performance of the aircraft design. The elliptic nose shape is thus selected for the SMR reference aircraft and is acknowledged as a good candidate to represent the nose shape.

2.1.3 Boundary layer sensitivity to mach number

To follow on the flow response due to changes in nose geometries, a further investigation is performed using the precedent hemispheric nose for different flight Mach numbers. At a glance, a distinctive trend arises where higher free-stream Mach numbers favour shock generation and thicken the BL. For flight conditions below transonic, i.e. M0.75, no shock is reported by the BL displacement area Δ^* . Whereas M0.65 and M0.70 flight conditions do not differ in the different charts of Fig. 6, at M0.75 the flow experiences a thicker BL from the aircraft shoulder suggesting a higher amount of energy imparted, not necessarily recoverable. The growth along the fuselage does not recover and suggests higher potentials from the momentum and energy defects. Above those conditions, a shock develops at the shoulder which eventually impacts its flow downstream and intensifies with respect to flight conditions. Nevertheless, this additional defect generated does not echo with a higher aerodynamic behaviour as can be explained by the kinetic energy deposition rate downstream of the body and its transfer into viscous dissipation rate. Not only the dissipation rate increases irrecoverably but the volumetric pressure work rises as the shocks and compressibility effects become more important. In practice, the overall power increase and the portion of pressure-defect work takes over the viscous dissipation rate due to the stronger shock.

2.2 Influence of the tail length and morphology

2.2.1 Rationale

Previous studies assessed the influence of the flight conditions on the energy recovery [16, 17]. More favourable effects are observed with the chord Reynolds number, body Mach number, angle-of-attack and body fineness ratio. For instance, Airbus Beluga-like aircraft suggest larger potential for energy recovery than slender bodies like the Airbus A380 and A320 families [16], but slender bodies retain quasi zero-pressure gradient dissipative characteristics over their surfaces and allow their approximations with flat plate theory. Despite investigations on the fuselage slenderness ratio, the influence of the tail fineness ratio on the BL properties and the potential energy recuperation has not been studied, and important considerations must be taken on the *quality* of the incoming airflow. It is preempted that the presence of the nacelle, when integrating a propulsor around the fuselage tail, impacts the flow before it passes through the fan. Therefore, the upstream flow needs to be further analysed as it is expected to highly impact the performance of the fan (with distortion and energy harvesting). On conventional aircraft, the rear-end of the aircraft is assimilated as a non-axisymmetric frustum (to prevent tail strike) whose trailing edge serves as an exhaust to the auxiliary power unit (APU). However, for the sake of simplification in this work and to focus on BLI aerodynamics, the requirements of tail-strike up-sweep and APU have been omitted, and the tail approximated with an axisymmetric cone.

2.2.2 Morphing sequence

First, different tail fineness ratios are defined on the conic tail. To maintain the aircraft's chord length, the mid-body fuselage length is extended accordingly. Whilst a retrofit integration of the BLI propulsor

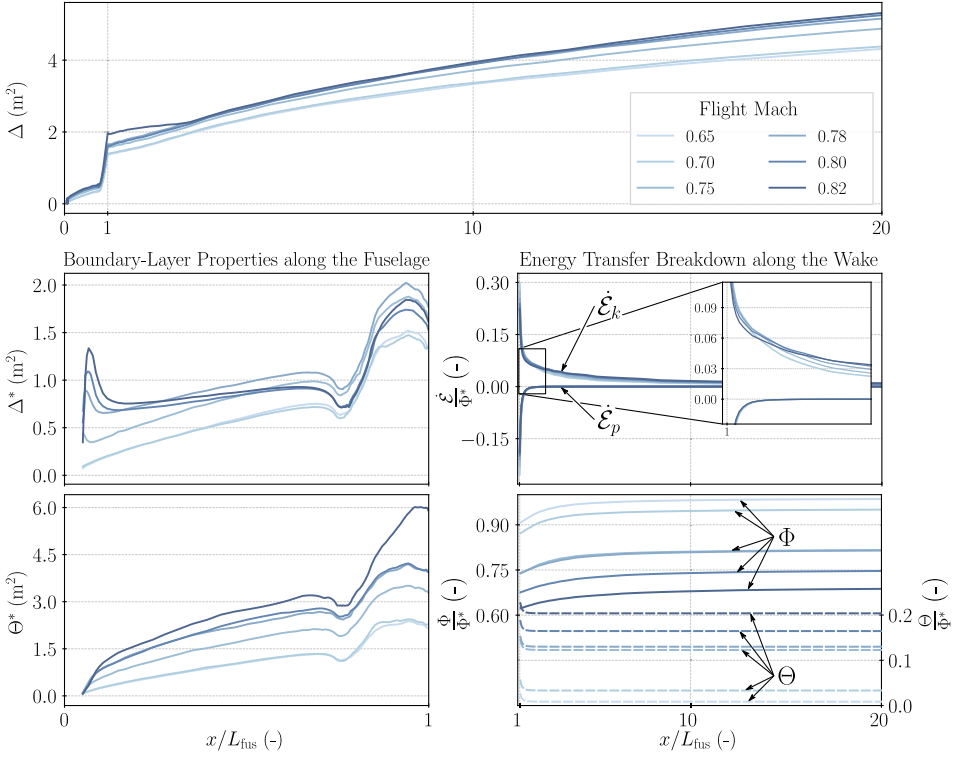


Figure 6. 3D axis-symmetric boundary-layer area (top), displacement area, momentum area and kinetic energy area (left) and wake energy-flux transfers and potential for energy recovery (right) for Mach numbers between 0.65 and 0.82 on the hemispherical nose approximation.

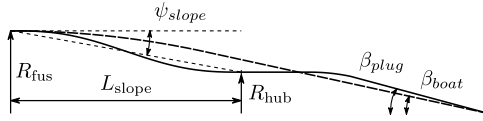


Figure 7. Tail morphing sequence from its reference (---) to its morphed shape (—), from Ref. [12].

around the conic tail can be performed [22], more tightly integrated propulsion systems necessitate a morphing of the tail to axially direct the flow through the fan. In doing so, some of the integration effects can be quantified by means of comparison with a bare morphed fuselage. This is a necessary stepping stone to decompose the installation effects, as to whether they are attributed to the morphing or nacelle inclusion.

To that end, the conical tail is used as reference whereby a serpentine substitutes the initial arc leading to the cone. This serpentine offers a natural extended pre-diffusion of the flow to better direct the flow towards the fan. Ensuring adequate spacing for the propulsor’s nacelle integration, the plug-cone features a shorter length with a steeper slope. An illustrative example is given in Fig. 7 following the morphing described.

Subsequently, Fig. 8 depicts a set of four conic tail designs (solid curves) and a morphed tail (dashed curve). The tail fineness ratio, FR_{tail} , is swept for a constant fuselage radius where the different tail lengths are reported from the shortest L1 to the longest L4. The closest approximation to the reference aircraft’s frustum is given by L2 which morphed tail equivalent is reported as L2’ in the following.

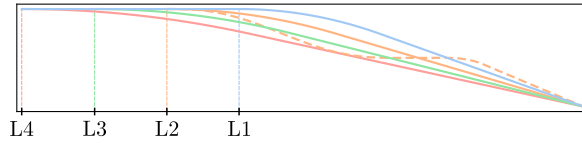


Figure 8. 2D axi-symmetric modelling of conic tail-cones of different lengths, and a morphed tail (dashed) derived from L2.

2.2.3 Figures of merit

In scenarios where no external force is given by either \mathcal{P}_s or \mathcal{P}_f , the fuselage drag power is deposited into the flow and transferred in different power forms as given in Equation (4).

$$-\mathcal{F}_{fus} \cdot \mathbf{V}_B = \dot{\mathcal{E}}_m + \Phi + \Theta \tag{4}$$

However, part of the mechanical energy-rate present in the BL is not entirely exploitable. To segment the recoverable part, the velocity at any point of the flow-field is decomposed into its isentropic and non-isentropic components [23]. Therefore, applying the decomposition in Equation (5), $\dot{\mathcal{E}}_m^*$ denotes the isentropic portion and $\overline{\dot{\mathcal{E}}_m}$ the non-isentropic portion of the mechanical energy.

$$\dot{\mathcal{E}}_m = \dot{\mathcal{E}}_m^* + \overline{\dot{\mathcal{E}}_m} \tag{5}$$

Introduced by Sanders and Laskaridis, the potential for energy recovery (PER) is used as a means of describing the portion of the BL flow rich in non-dissipated energy potentially extractable by a mechanical device. Initially defined in Ref. [4] with the viscous dissipation rate at the trailing edge of the bare fuselage Φ_{TE} (Equation (6a)), the definition is later corrected in Ref. [24] and approximated to account for the irreversible compressibility-induced losses Θ_∞ (Equation (6b)). These two definitions are volumetric integrals and do not enable the accumulation of PER to be tracked along the surface. In Ref. [17], the accumulation of the non recoverable energy $\overline{\dot{\mathcal{E}}_m}$ relative to the overall energy-rate deposited by the fuselage can be quantified at any given survey plane along a surface or in the wake (Equation (6c)). Using the velocity decomposition method, it is now possible to apply the strict definition of PER whereby the irreversible compressibility-induced losses $\Theta_{irr,TE}$ are not approximated with their residual value (Equation (6d)). In essence, Θ is split in its reversible and irreversible components from a power balance re-arrangement, and the ideal maximal energy recovery is quantified.

$$PER_{Sanders} = 1 - \frac{\Phi_{TE}}{\mathcal{F}_B V_B} \tag{6a}$$

$$PER_{Lamprakis} = 1 - \frac{\Phi_{TE} + \Theta_\infty}{\mathcal{F} V_B} \tag{6b}$$

$$PER_{Mutangara} = \frac{\overline{\dot{\mathcal{E}}_m}}{\mathcal{F}_B V_B} \tag{6c}$$

$$PER = 1 - \frac{(\Phi + \Theta_{irr,TE})}{\mathcal{F}_B V_B} \tag{6d}$$

2.2.4 Aerodynamic sensitivity

To characterise the flow sensitivity to changes in the plug-cone shape, Fig. 9 depicts the BL area and its kinetic energy area along with $PER_{Mutangara}$ for all conic tails and its morphed derivative. It appears that the longer the fuselage mid-section (i.e. the shorter the tail), the slightly thicker the BL and its excess properties along the mid-body as the wetted area increases and more energy is deposited into the flow.

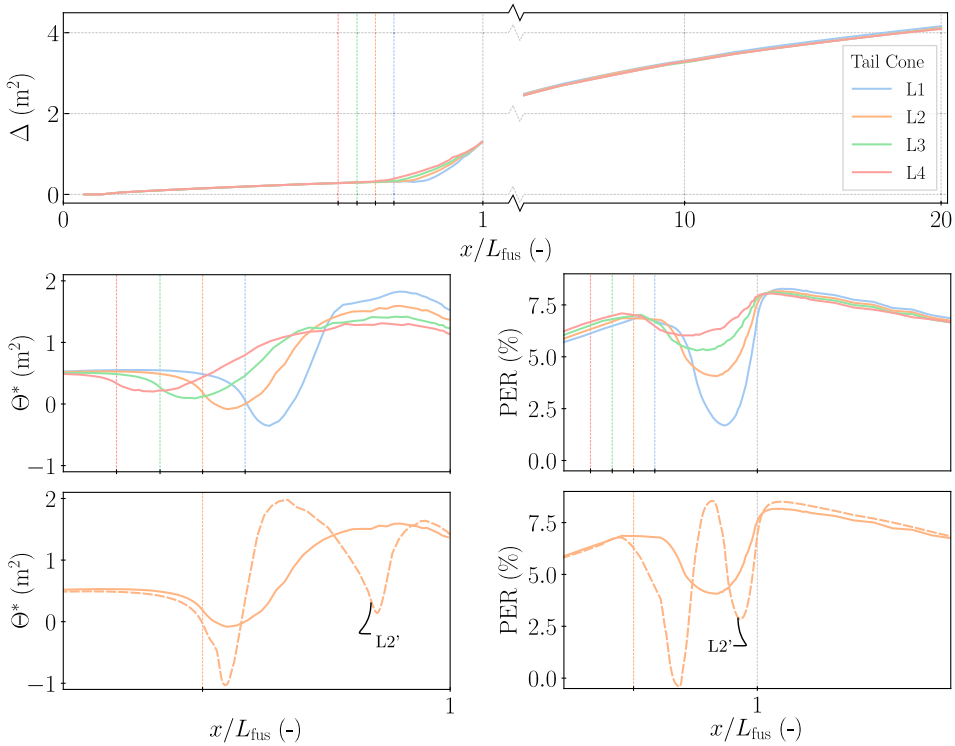


Figure 9. 3D axi-symmetric boundary-layer area (top), kinetic energy area (left) and potential for energy recovery from Equation (6c) (right) for the four conic tails of different lengths and a morphed derivative at FL350 and $M_B = 0.82$.

These discrepancies are nonetheless quite negligible at the trailing edge but play an important role as the flow experiences different pressure gradients around the tail.

First, as the BL flow approaches the tail (represented by the vertical dashed lines for the different tails), it is dragged down to follow the body's curvature which locally accelerates before diffusing and decelerating along the slope as it experiences an adverse pressure gradient. For instance, L1 experiences a steeper boat angle than L4 causing a sharper rise in velocity around the convex fuselage region therefore contributing towards a local defect in energy as the velocity at any point within the BL is larger than its edge quantity.

The comparison of the conic tail L2 with its morphed derivative L2' follows in the last row of Fig. 9 whereby an important drop in BL properties is experienced before a sharp bounce back. This phenomenon is justified by the steeper change in geometry curvature which then plateaus – to later integrate the propulsor, and then a replica of the precedent curvature at the plug-cone. This double phenomenon in BL properties results from two strong favourable pressure gradients intertwined by adverse gradients. However, the last drop in Θ^* is smaller in amplitude than the previous as the flow pre-diffused. It is opined that the consideration of either cone shape has an impact on the BL properties at any location along the tail and results in a benefit in excess mechanical energy that can be harvested by a device.

Tracking the accumulation of the non recoverable energy relative to the overall energy-rate deposited by the fuselage, PER is quantified at any given survey plane along the wall surface, and in the wake. Nonetheless, despite allowing one to track the accumulation of energy deposition rate that can be harvested mechanically, and being a contribution to this paper, the progress of PER along the body is subject to several factors. Its comparison with the definitions from previous works [4, 24], given in Fig. 10, yields significant discrepancies. Notably, larger differences for L1 than for L4 are explained by shorter and steeper boat tails which cause adverse pressure gradients and affect the reported accumulation of

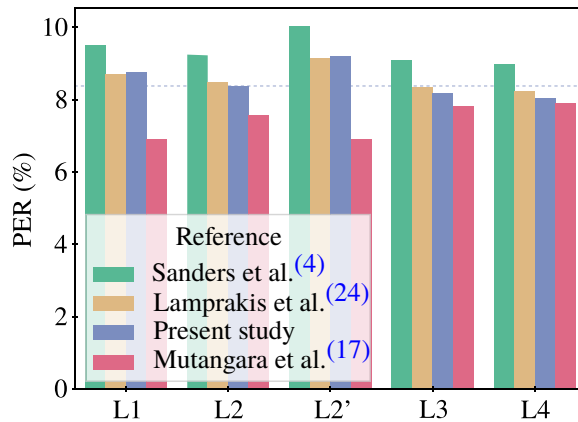


Figure 10. Comparison of the potential for energy recovery refinement definitions on the different tails from Figure 8 at the fuselage trailing edge, with the PER value of the present study (Equation (6d)) on the tail L2 given in a dashed line for ease of comparison.

$\overline{\mathcal{E}}_m$ as seen with Fig. 9. These pressure gradients are responsible for large deviations given in Θ and predominantly in its reversible component Θ_{rev} . This sharp rise in Θ is the result of a larger isentropic compression and dilation process captured by the other definitions reported in Fig. 10. Additionally, a delay is noted between the kinetic energy area Θ^* and PER. This is caused by the difference in survey plane definitions. In the former, planes perpendicular to the wall surface are used to the BL edge to determine the BL properties whereas vertical surveys are defined in the decomposition method to sweep over the entire domain height. Lastly, the fineness of the meshes generated alter the decomposition yielding higher numerical dissipation. As the tail length increases, slender aft-bodies experience lower pressure gradients but generate viscous dissipation as a result of shear stresses along the wall surface. Despite ensuring fine meshes to capture the viscous sub-layer, this turbulent region would need very fine grids to decompose well the velocity components. However, it is found that the viscous dissipation rate is highly sensitive to the mesh fineness and non-dimensional first cell heights y^+ below one underestimate its value.

Overall, a decreasing trend in PER values is noted with respect to the tail length. The comparison of the conic tail with its morphed derivative yields a larger recovery potential as postulated. The concave diffusive slope imparts more energy to the flow (thanks to a larger fuselage drag power) which does not dissipate upstream of the survey plane and reports larger mechanical benefits.

Morphed geometries locally favour pressure-defect work over viscous dissipation, contributing to larger PER (Fig. 10). This can be explained by the increased dilation from changes in curvatures and the larger wetted area. Nonetheless, all the energy is not transformed into Θ or Φ leaving a greater aerodynamic potential as given by PER. Importantly, it is reminded that greater potentials do not necessarily translate to greater benefits. Figure 11 depicts that transfer of energy between L2 and L2' whereby slightly smaller diffusive effects are observed for the morphed tail region. It appears however clear that at the fuselage trailing edge, the non recoverable energy $\overline{\mathcal{E}}_m$ is slightly under-predicted, as previously mentioned, and therefore negatively impacts $PER_{Mutangara}$ value, which can still be used as a conservative approach. With the integration of a propulsor which fan could be placed around 50–60% of the tail length (Fig. 9), ingesting the bottom layer of the BL rich in energy would reduce the fan power requirement to operate as well as reduce the integration penalties, e.g. over-cowl viscous dissipation. However, as expressed before, the pressure gradients faced by the flow locally affect PER around the mid tail to a larger extent with the conic than the morphed tail. Despite advising to integrate a thruster around the middle of the morphed tail, the morphology plays an important role in the recoverable work and the fan size still needs to be assessed.

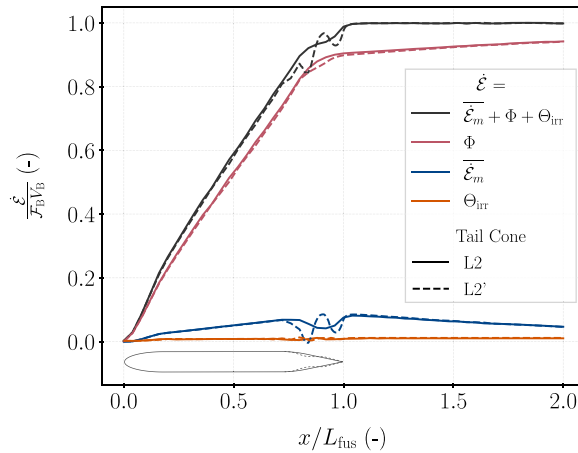


Figure 11. Energy decomposition and their evolution along the fuselage surface and in the mid-field wake.

2.3 Influence of the morphed shape

2.3.1 Slope angle effects

Unlike the previous investigation on the conic tails with their derivation in a morphed candidate, the flight speed is reduced to $M_B = 0.78$ ($Re = 2.73 \cdot 10^8$) for the rest of the paper to agree with the cruise mission of the PFC and determine a morphed baseline at its condition. To understand the influence of the shaping, morphed fuselages are designed with different combinations of slope lengths and angles. First, the pre-diffusive slope is investigated to help direct the flow before entering the propulsor. As such, the slope angle is defined as $\psi_{slope} = L_{slope} / (R_{fus} - R_{hub})$ between the tail starting point at the fuselage radius and the hub radius of the envisaged propulsor throat position, marking the end of the slope.

Each fictitious position of the propulsor's throat is discretised in 40 survey planes equi-spaced from the fuselage wall to the BL edge, where the mass-flow averaged Mach number and mass-flow rate are computed. Figure 12 reports the Mach number relative to the fan-face target to ensure its operation with respect to all morphed tail slope angles ψ_{slope} to depict the influence of the pre-diffusive slope. The cloud bounds the Mach number extrema for target ingestions of 20–100% of the BL mass-flow, following a kernel distribution. Inside it, the mid-height scatter quantifies the mean Mach number of this design, and its surrounding box covers the 25th to 75th quartiles which extend with matches representing the extrema (not including outliers). Additionally, a filter is applied on the mass-flow rate integrals to ensure that no reverse flow is captured at the axial position which would enlarge the throat area to capture the target mass-flow rate and increase the load and distortion faced by the fan.

For ψ_{slope} larger than 13° in Fig. 12, more than 75% of the calculated Mach numbers on the survey planes fall below the 90% threshold defined. To ensure the condition is met at the fan on these designs, its size should be large enough to ingest enough mass-flow, and its intake should undesirably be designed convergent to locally accelerate the flow generating larger total pressure distortion. Therefore, morphed fuselages which slope angles causing Mach numbers to fall under the threshold as well as Mach numbers that will lead to only large propulsors are discarded, and their integrated propulsive concepts not designed.

Conversely, for designs leading to Mach numbers close to the target, propulsor integration effects will naturally slow down the flow before crossing the intake towards the fan. As for the designs with Mach numbers above the target, additional diffusion is ensured within the propulsor intake to reduce the flow speed.

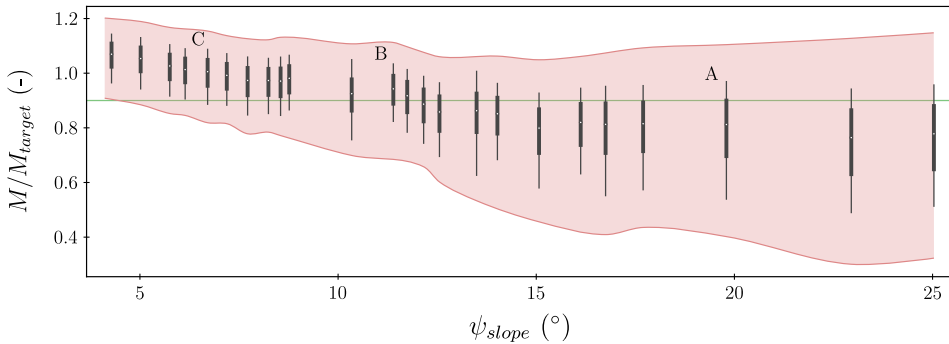


Figure 12. Distribution of mass-flow averaged Mach numbers at the slopes' end-points with respect to different inclination angles, with 3 identified designs for later use, relative to a threshold of 90% of the Mach number target.

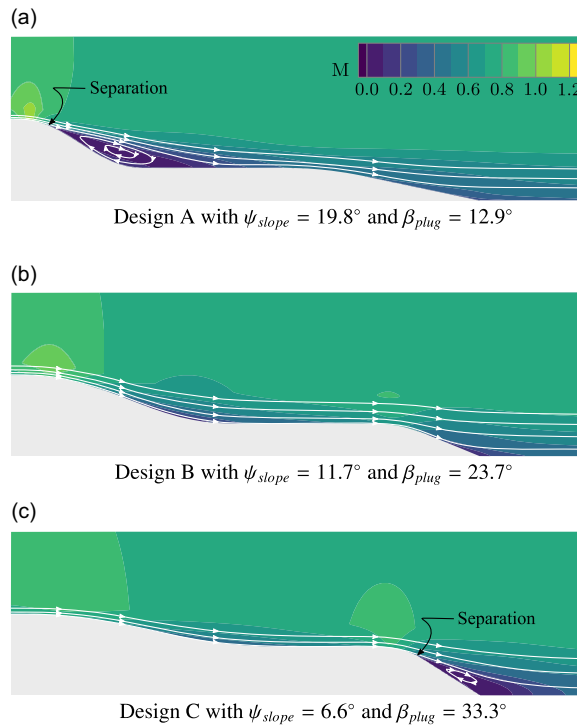


Figure 13. Computed Mach number contours around the three designs identified in Fig. 12.

2.3.2 Plug angle constraints

In addition to the constraints on the slope angle, the integration of the propulsor along the tail directly constrains the plug length (for a given tail length) as well as its angle (with respect to the slope angle). As such, if the change in curvature is too important, the flow separates downstream of the fuselage impacting its aerodynamic performance. Through the integration of the retrofit propulsor around the morphed tail, the flow exiting the exhaust at a higher speed than the bare fuselage will also likely separate. To prevent the generation of these propulsive designs, the pressure and skin-friction coefficients are tracked along the plug surface. The absence of friction on a body's surface suggests a flow separation, and as a by-product a sharp rise in the pressure coefficient. To illustrate, the flow-field around the tail's plug is reported in Fig. 13 for the three designs previously identified in Fig. 12.

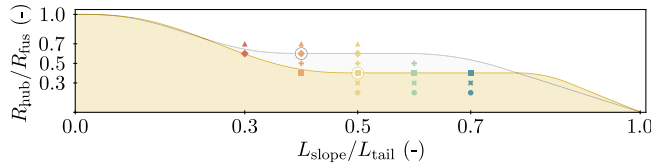


Figure 14. Schematic of two morphed fuselages for $L_{\text{slope}}/L_{\text{tail}} = 0.4$ and 0.5 , and $sR_{\text{huba}}/R_{\text{fus}} = 0.6$ and 0.4 , respectively, in grey and yellow with \bigcirc .

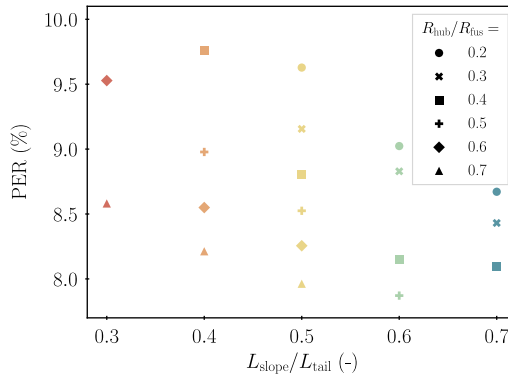


Figure 15. Potential for energy recovery with respect to the different slope lengths and hub radii given in Fig. 14.

As a result of separation on Fig. 13(a) for $\psi_{\text{slope}} = 19.8^\circ$, the Mach numbers and mass-flow rates computed for Fig. 12 suggested reversed flow on the survey planes which disregarded the designs previously identified. Conversely, for Fig. 13(c) with $\psi_{\text{slope}} = 6.6^\circ$, a large majority of the flow conditions computed fell above the fan requirements, but could be balanced with a well-design propulsor intake. On these designs, the plug length is constrained (as the tail length is imposed) featuring a steep angle of $\beta_{\text{plug}} = 33.3^\circ$, showcasing separation downstream of the fuselage. Following the fair assumption that separation will remain for powered aircraft, fuselages like design C are also disregarded. Consequently, when both slope and plug angles fall below their critical angles, flow-fields similar to the design B in Fig. 13(b) are obtained.

Retrieving Fig. 12, the design space is bounded by the critical slope angle and its induced plug angle between 7 and 13° , with steep plugs and steep slopes, respectively. These designs are represented in Fig. 14 where designs like A are removed from the bottom-left corner, and like C from the top-right corner (missing scatters).

2.3.3 Slope length and hub radius effects

Further to the narrowed-down morphed fuselages and from the possibility of tracking PER along the fuselage, the definition from Mutangara et al. [17] is followed. Based on the designs given in Fig. 14 with respect to different hub radii and slope lengths (in markers), $PER_{\text{Mutangara}}$ values are reported in Fig. 15.

As expressed above, more aggressive slope designs provide additional energy to the viscous flow, locally present in the form of pressure, with low shear stresses hence contributing to higher PER values as viscous dissipation is delayed. This phenomenon is observed where the slope length is constrained to low values featuring a somewhat sharp ramp. With increasing slope lengths, PER decreases as more streamlined flows experience larger shear stresses responsible for viscous dissipation. For the same reasoning, low hub radii favour PER as the rise in energy deposition rate is not yet converted into irrecoverable losses. In addition, the monotonicity in PER with hub radii is respected regardless of the slope length.

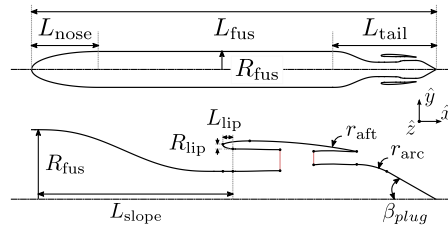


Figure 16. Schematic of an axi-symmetric fuselage with a thruster at its tail featuring a pre-diffusive slope, propulsor intake, cowl, exhaust, and aft-cone, from Ref. [12].

Lastly, the uneven distribution for $L_{\text{slope}}/L_{\text{tail}} = 0.4$ and 0.6 is observed as the lowest hub radius of the former axial location does not experience reverse flow but is still subject to a strong pressure gradient contributing to $\dot{\mathcal{E}}_p$ locally, increasing the perceived PER. Conversely for the latter location, the opposite is observed for higher radii where the somewhat steep plug angle affects the mechanical energy-rate terms at the survey station and reduces the potential for energy recovery.

3.0 Propulsor integration: propulsive fuselage concept

3.1 Propulsor parametrisation

Propulsors are circumferentially mounted around the aft-end morphed fuselages with a fan and its encapsulating nacelle. Figure 16 depicts the propulsive fuselage concept with its macro positioning parameters ensuring that the constraints associated with the reference fuselage are not violated. The new geometry embeds a propelling fan and casing similar to existing concept with a serpentine pre-inlet outline (5th polynomial Bell-Mehta [25]) in lieu of tapered [7] or smooth S-shaped⁽⁸⁾ slopes. As the integration of the BLI propulsor must guarantee a pre-diffusion whilst avoiding any flow recirculation upstream of the nacelle, a Bell-Mehta fifth-order polynomial is used as a versatile and robust implement [25] to direct the inflow. The propulsor parametrisation follows a combination of Bell-Mehta polynomials, circular and elliptic arcs and a fore-cowl NACA-1 Series [26].

3.2 Integration effects

To evaluate the influence of the propulsor integration, two candidates are integrated to ingest only the sub-viscous layer (around 25% of the BL mass-flow) and the entire BL mass-flow, and compared with the clean flow over their morphed fuselage. An example of this installation is given in Fig. 17 with the clean morphed tail represented with dashes (from Fig. 14 in yellow) and a fictitious nacelle. It was identified by Gray et al. a growth of the boundary-layer thickness by 15 and 25% between the clean flow (unintegrated tapered tail) and two propulsors of different sizes [7]. Herein, the two designs in Figs 18(a), and (b) are considered where the BL thickness grows by respectively 4 and 8% at $x/R_{\text{HL}} = 0$, or an increase in 12% and a decrease in 4.3% in mass-flow rate relative to the morphed fuselage, respectively.

Reference [7] reports the sensitivity of the aerodynamics to FPR for a constant fan power input, where the fan diameter and its pressure ratio (or rotational speed) have an inverse relationship whereby a larger fan rotates more slowly and compresses less the air through its stage. The integration effects upstream are therefore subject to changes in the fan and propulsor sizes rather than only its pressure ratio, as stated in Ref. [7], as the nacelle lip is shifted vertically up or down. The speed reduction along the tapered tail extends one propulsor radius upstream of it whereas in serpentine geometries, Figs 18(c) and (d) suggest that these penalties are dependent on the propulsor size. For the two geometries considered, the aerodynamics is affected one highlight radius upstream of the nacelle ($x/R_{\text{HL}} = 1$) for the small propulsor whereas as the size increases, penalties occur up to two highlight radii upstream ($x/R_{\text{HL}} = 2$). These differences from Ref. [7] are a direct result of the tail morphology which is more subject to local

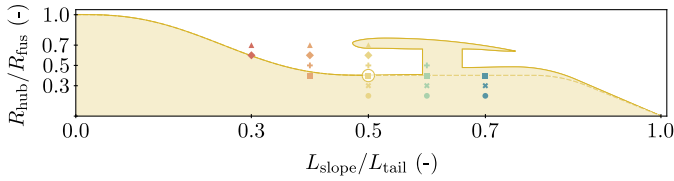


Figure 17. Schematic of an integrated propulsor (—) at $L_{\text{slope}}/L_{\text{tail}} = 0.5$ and $R_{\text{hub}}/R_{\text{fus}} = 0.4$ ingesting 60% of the mass-flow present in the boundary layer, as denoted with \bigcirc , from its morphed fuselage (--) in Fig. 14.

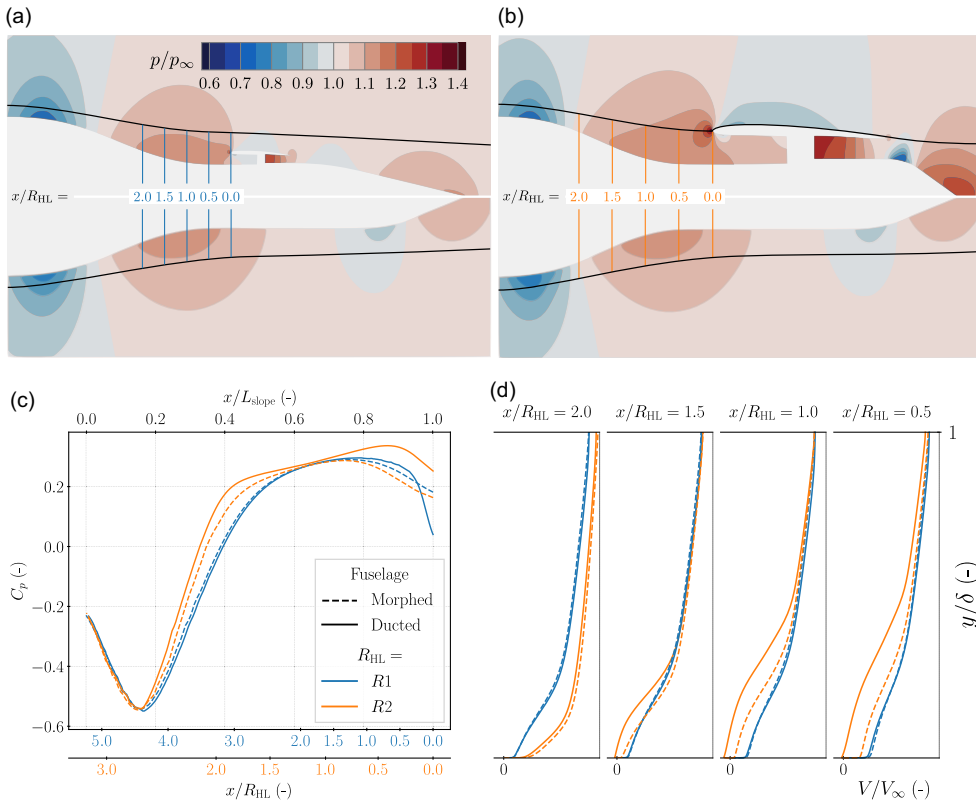


Figure 18. Comparison of normal static pressure (a) for a propulsor ingesting only the sub-viscous layer (—) and (b) for a propulsor ingesting the entire boundary layer (—), and comparison of (c) pressure coefficients and (d) velocity profiles along the fuselage slopes between the morphed and the ducted geometries at the same position (Fig. 17) from the propulsor highlight axial position. Integration effects upstream are reported as fractions of the propulsors highlight radii.

effects. Notably with the large throat, the flow is pushed further forward up to half the BL thickness as a result of the adverse pressure gradient from the nacelle lip faced (Figs 18(a) and (b)), and these effects reduce in height further away from the highlight, reversing the flow very close to the wall surface in some cases (Figs 18(c) and (d)).

Overall, the observations made on the local integration effects upstream of the propulsor agree with those from Gray et al. despite their tapered tail geometry and operating at a lower vehicle speed ($M_B = 0.72$):

- the boundary layer thickness grows with the integration of a propulsor;
- this growth further increases with respect to the propulsor diameter;
- the lower half of the boundary layer experiences a speed reduction up to 2 highlight radii upstream of the nacelle;
- this speed reduction is correlated with the propulsor diameter;
- the local pressure gradients caused by the propulsor integration propagate farther upstream than the changes in the velocity profiles.

3.3 Aero-propulsive performance metrics

The turbo-electric architecture used in PFC requires the main turbofans mounted under the wings to generate part of the aircraft thrust demand whilst the power from the low-pressure turbines is extracted to feed the aft-mounted thruster. Therefore, to evaluate the aero-propulsive performance of all candidates, the overall power consumption needs to be calculated and compared against a reference. To maintain the same steady-level cruise mission than the reference aircraft, the fuel-flow rate is used as performance metric. In that respect, the investigations are only performed at design point where the power saving coefficient (PSC), a surrogate of fuel savings, is reported. Additionally, the share of propulsive force between the thruster and main turbofans is given by the propulsive force share (PFS) as the ratio of the force produced by the aft-mounted fan relative to the overall aircraft requirement.

3.3.1 Power consumption and savings

In this work, retrofit state-of-the-art turbofans designed by Zhao and Yao [27] and comparable to the CFM LEAP-1 or PW1100G are used. Therefore, all PSC values reported under-estimate the real savings the novel aircraft might achieve as in real case scenarios, the main turbofans should be down-scaled as less thrust is required from them. Notably, there would be additional savings on nacelle drag and weight (albeit the latter is not considered here). Nevertheless, this approach allows one to compare all propulsor designs generated in a similar manner by only assessing the benefits from the thruster and not considering any further aero-propulsive benefits from the re-scaling.

To that end, the shaft power \mathcal{P}_S from the power balance in Equation (2) describing the aft-mounted fan power demand is given as \mathcal{P}_{BLI} to differentiate it from the main turbofans \mathcal{P}_{pod} :

$$\mathcal{P}_{\text{BLI}} = \iint_{S_p} \left[\rho \left(e + \frac{\mathbf{V}^2}{2} \right) \mathbf{V} + p\mathbf{V} - \bar{\boldsymbol{\tau}} \cdot \mathbf{V} \right] \cdot \hat{\mathbf{n}} dS \tag{7}$$

In the turbo-electric aircraft architecture considered, this energy is an electrical power demand which needs to be first converted from mechanical energy, as extracted from the low-pressure turbine (LPT) of the under-wing turbofans. However, this modelling is out of the scope of this paper and rather, a transmission efficiency is introduced as η_{trans} . The actual power extracted from the low-pressure shaft is given in Equation (8) and related to the overall power consumption \mathcal{P}_{PFC} in Equation (9):

$$\mathcal{P}_{\text{BLI,PFC}} = \frac{\mathcal{P}_{\text{BLI}}}{\eta_{\text{trans}}} \tag{8}$$

$$\mathcal{P}_{\text{PFC}} = \mathcal{P}_{\text{pod,PFC}} + \mathcal{P}_{\text{BLI,PFC}} \tag{9}$$

whereby $\mathcal{P}_{\text{pod,PFC}}$ accounts for two turbofans mounted on either sides.

Relative to the reference aircraft that only produces the required forward force, the power saving coefficient is defined with:

$$\text{PSC} = 1 - \frac{\mathcal{P}_{\text{PFC}}}{\mathcal{P}_{\text{A/C,ref}}} = 1 - \frac{\dot{m}_{f,\text{PFC}}}{\dot{m}_{f,\text{A/C,ref}}} \tag{10}$$

which is reducible to the right-hand side formulation with \dot{m}_f denoting the fuel-flow rate, assuming that the same fuel properties are considered in both aircraft.

In this work, the latter formulation is used based on engine decks for combinations of power off-takes and propulsive force generation. To that end, the fuel saving coefficient (FSC) is used in lieu of the PSC but represents the same metric.

3.3.2 Propulsive force share

In the PFC, the propulsive force is split in between the under-wing engines and the aft-mounted thruster. The portion of force generated from the latter relative to the main turbofans is given by the propulsive force share (PFS):

$$\text{PFS} = \frac{\mathcal{F}_{\text{BLL,PFC}}}{\mathcal{F}_{\text{PFC}}} \quad (11)$$

This non-dimensional form shows its importance when one designs different aircraft and evaluates the change in propulsive force under equivalent power supply, or inversely, the change in power requirement to maintain the same force. The overall force requirement from the PFC (\mathcal{F}_{PFC}) is estimated from a drag build-up isolating the propulsive fuselage from the rest of the aircraft [12]. All forces \mathcal{F} are computed from near-field integration of pressure and friction around wall surfaces:

$$\mathcal{F} = \iint_S (p - p_\infty) \hat{n} - \bar{\tau} \cdot \hat{n} dS \quad (12)$$

To obtain the direct contribution of the propulsive fuselage, the forces $\mathcal{F}_{\text{fus+P,PFC}}$ on the propulsive fuselage are compared against the morphed clean fuselage $\mathcal{F}_{\text{fus,PFC}}$ previously used by associating in change in force distribution to the propulsor integration:

$$\mathcal{F}_{\text{BLL,PFC}} = \mathcal{F}_{\text{fus+P,PFC}} - \mathcal{F}_{\text{fus,PFC}} \quad (13)$$

4. Novel aircraft aero-propulsive performance evaluation

4.1 Propulsor position effects on aero-propulsive performance

Following the observations and recommendations made on the clean morphed fuselage, the macro parameters (slope length, hub radius, throat area and fan pressure ratios) are explored in a systematic approach. Following the nomenclature from Fig. 17, Fig. 19 depicts the global pareto between the propulsive force and the power savings for the different slope lengths $L_{\text{slope}}/L_{\text{tail}}$ and hub radii $R_{\text{hub}}/R_{\text{fus}}$ with respect to different propulsor sizes and fan operating conditions. It is reminded that the fuel savings are calculated between the novel aircraft featuring retrofit turbofans (operating at off-design) and the reference aircraft. Therefore, all savings reported are under-estimated in terms of the propulsor resizing, but probably overestimated from other aspects, like weight estimations, transmission efficiency, and 3D aerodynamics of the flow due to tail-cone up-sweep.

With respect to the positioning of the propulsor along the tail, two main categories are observed. First, for tails with short slopes (red and orange markers), the best performance is obtained for large hub radii (diamond and triangle markers). This confirms the observations made on the slope angle whereby, when constrained in length, the slope's end-point radius must be sufficiently high to prevent flow recirculation upstream and provide a homogeneous flow distribution at the AIP for a target Mach number. With these designs, a long streamlined plug-cone prevents separation and a recirculation bubble behind the fuselage. Conversely, for long slopes (green and blue markers), a low hub radius (circle and cross markers) offers a natural flow pre-diffusion whilst guaranteeing a relatively low plug angle for better force distribution, i.e. forward force production. Whilst the mid-length of the tail regroups all propulsors in the 4 to 10% FSC and 10 to 60% force share, a larger force contribution from the thruster reduces the savings. Steeper plug angles contribute to larger force generation with propulsors ingesting more mass-flow but require larger power demands yielding less benefits claimed from BLI.

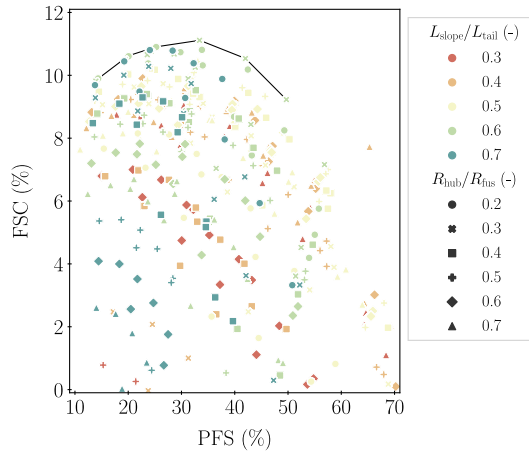


Figure 19. Overall performance of a propulsive fuselage concept for various BLI propulsor positions along the aircraft tail, with symbols following Fig. 17 convention.

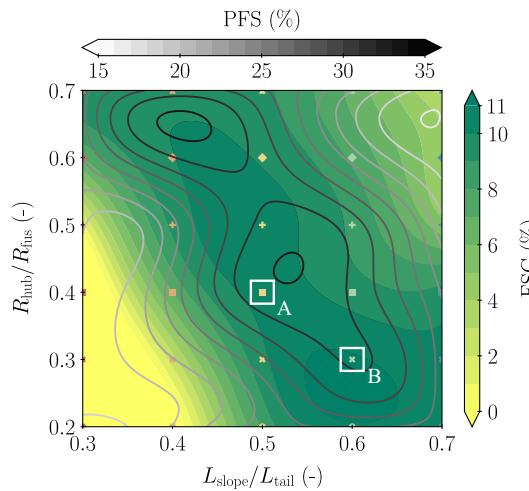


Figure 20. Computed contour map of a propulsive fuselage concept overall performance for various BLI propulsor positions along the aircraft tail.

To depict the best performing candidates of each marker combinations, Fig. 20 maps out the best PFS and FSC at each propulsor location. For the given combination of slope lengths and hub radii, the different propulsor sizes and fan operating conditions are compared to down-select the best fuel savings. As suggested, optima bound the PFS between 15 and 35% of the aircraft thrust requirement to maintain its steady cruise segment.

The largest force shares are split into two locations also yielding large savings:

- at high hub radial positions (≈ 0.65) for short slope lengths (≈ 0.40) but these bulky designs would increase the aircraft mass whilst potentially favouring flow separation upstream of the nacelle at high angles of attack;
- at a mid-to-low hub radial position (≈ 0.40) for mid-range slope lengths (≈ 0.55) where milder weight penalties are envisaged and pre-separation prevented.

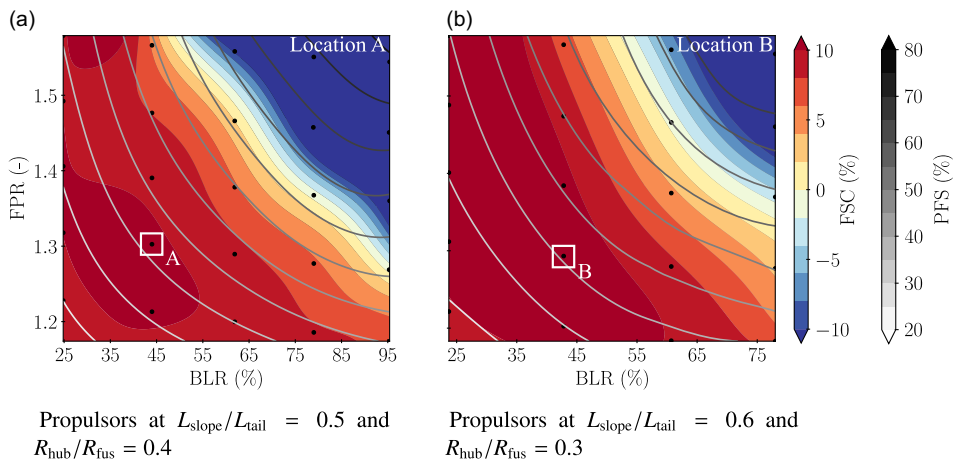


Figure 21. Computed contour maps of a propulsive fuselage concept overall performance for various BLI propulsor operating conditions at two different positions along the tail.

Nonetheless, by zooming in this latter region, the propulsive forces generation require different intensities of power to run the fan. In that respect, the highest savings are obtained at slope lengths around 60% of the tail length for low hub radii as the sub-viscous boundary layer is rich in energy. Also, there are fairly similar savings for a broad PFS and it would probably be better to operate on the lower PFS range, because this would incur less penalties later on when weight of the system and transmission efficiency are considered.

4.2 Influence of propulsor size and operation

Retrieving the two combinations of PFS and FSC identified as A and B from Fig. 20, Fig. 21 gathers the aero-propulsive performance differences at $L_{\text{slope}}/L_{\text{tail}} = 0.5$ and $R_{\text{hub}}/R_{\text{fus}} = 0.4$, and at $L_{\text{slope}}/L_{\text{tail}} = 0.6$ and $R_{\text{hub}}/R_{\text{fus}} = 0.3$, for different boundary layer ratios (BLR), ratio of mass-flow rate ingested relative to the entire boundary layer and the fan pressure ratio, FPR.

Notably, an inverse relationship between PFS and FSC is observed whereby lower combinations of BLR and FPR provide important savings ($\approx 10\%$) for maximum a third of the overall aircraft's force production. This intuitive result translates the BLI beneficial effects whereby a great amount of energy is harvested from the fan to which small power input is provided to mitigate the wake losses whilst generating a forward force. With increases in BLR and FPR variables, larger forces in the forward direction are achieved but to the cost of power savings. Similar patterns are obtained at both locations but geometric constraints on the plug-cone prevent high BLR propulsors in Fig. 21b. At constant FPR, the ingestion of larger mass-flow rates across the fan returns less benefits as the energy present in the flow asymptotes to zero in the absolute reference frame. Therefore, to maintain the pressure rise across the fan stage, greater power consumption is required yielding diminishing returns. Larger FPR's provide a compound effect on the force share whereby its gradient is greater than at low FPR for larger fan diameters.

Conversely, for a given fan design, an increase in its rotational speed increases the pressure rise with greater power inputs. Smaller propulsors nested inside the fuselage tail feature low-diameter fans harvesting all benefits from the sub-layer whilst producing a mild amount of propulsive force. With larger diameters, less benefits are harvested and larger penalties are imparted from the large wetted area of the nacelle cowl. However, larger portions of forward force are enabled. Therefore, it is of interest to investigate the potentials benefits offered by compact nacelles even if it is pre-empted to increase the levels of distortion at the fan-face despite potentially be balanced out by smaller aerodynamic penalties around the nacelle.

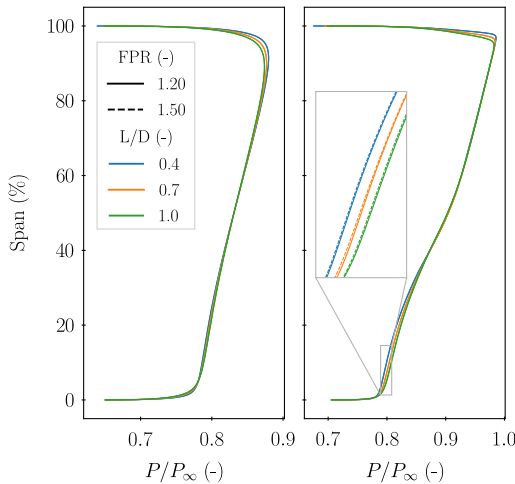


Figure 22. Normalised distribution of the total pressure along the fan span for the small propulsor R1 (left) and large propulsor R2 (right) under two fan pressure ratio and three intake lengths.

4.3 Benefits of compact nacelles

4.3.1 Intake length reduction

Larger distortion is experienced by a thruster fan than with a clean free-stream flow ingested by a turbofan mounted under the wings [15]. Despite the larger distortion, the pre-diffusion ensures a homogeneous circumferential flow distribution to the throat and only the radial distribution (span-wise) is investigated. In events where the pre-diffusion is not sufficient for the flow to reach the target Mach number at the fan-face, further diffusion is obtained from the intake design. With the consideration of compact nacelles around the propulsors, the total pressure distribution and radial distortion index (RDI) [28] are studied as complex flow diffusion from the intake and acceleration from the fan are combined.

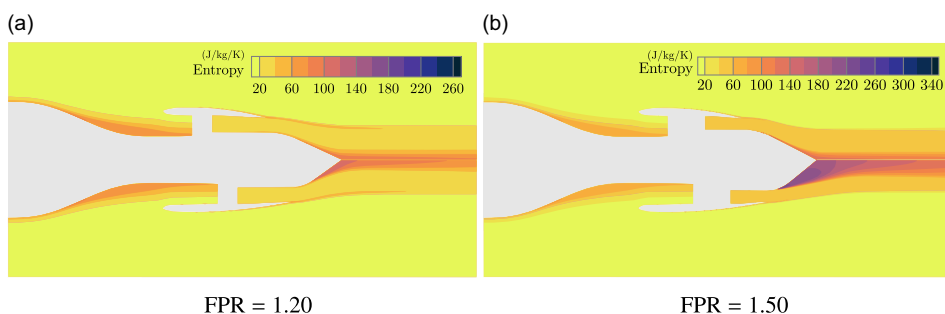
Both propulsor designs from Fig. 18 are investigated whereby 25% and 100% of the BL mass-flow are ingested. Short intakes are considered where the length over diameter ratio (L/D) is reduced from 1 to 0.7 and 0.4, respectively. In comparison, state-of-the-art under-wing engines' intakes range between 0.65 and 0.85 for SMR aircraft [29] whereas short intakes are designed around 0.5 [30].

Figure 22 depicts the distribution of the total pressure at the fan-face normalised by the free-stream total pressure for two propulsor sizes under the different intake lengths and fan pressure ratios. Similarly for both propulsor throat sizes, an increase in intake compactness sees the AIP pushed further forward (i.e. closer to the throat) increasing the total pressure distribution close to the nacelle shroud. Notably on the larger propulsor, suction effects in the lower region caused by larger fan pressure ratios reduce the total pressure distribution as the flow is slightly accelerated. Closer to the tip, the same phenomena are observed on all propulsors whereby larger diffusion, i.e. total pressure, occurs for longer intakes but the BL forming on the interior of the nacelle reduces the total pressure distribution.

As regards the RDI, values are reported in Table 1. For the different propulsors considered, increases between 10 and 14% in RDI are observed when the intake L/D is reduced from 1.0 to 0.4. Although these increases are non-negligible and at the fan designer's discretion [31], in this study the fan is modelled with ideal boundary conditions and therefore not transporting the experienced distortion through the fan stage which would be expected to increase the viscous dissipative losses. As degrees of fidelity are increased in the fan modelling, one should not omit the distortion effects and adjust the compactness of the intake to mitigate them.

Table 1. Radial distortion indices for two propulsors' intake dimensions and two fan pressure ratios

R_{HL}	FPR = 1.20			FPR = 1.50		
	L/D = 1.0	L/D = 0.4	Δ (%)	L/D = 1.0	L/D = 0.4	Δ (%)
R1	0.0399	0.0455	+14.0	0.0401	0.0456	+13.7
R2	0.0865	0.0954	+10.3	0.0869	0.0957	+10.1

**Figure 23.** Contours of entropy around large propulsors (R2) ingesting the entire boundary layer under fan pressure ratios of (a) 1.20 and (b) 1.50 for two intake/nacelle/plug-cone length combinations.

4.3.2 Plug-cone extension

From the geometries studied above and their intake length reductions, the nacelle lengths are reduced by the same amount to maintain an equivalent exhaust than the baseline. Consequently, this elongates the plug-cone and reduces its angle. For small propulsors, the reduction in nacelle length does not impact considerably the plug shape and its effects on the surrounding flow-field. However, with larger propulsors, the elongation offered in the plug-cone prevents abrupt curvature changes with smaller plug angles and favours the force distribution.

Notably, Fig. 23 depicts the large propulsor operating at two fan pressure ratios for the baseline and compact nacelles. Shrinking the propulsor's nacelle enables the plug-cone length to be extended and its angle to be reduced from 35.8 to 25°. The reduction in angle yields a smaller entropy generation behind the cone but not necessarily a better force redistribution on the plug arc and cone. As the jet velocity increases with FPR, the flow is more unlikely to remain attached to the wall surface and reducing the plug angle positively contributes to the net axial force. Notably, at low FPR, the reduction in plug angle from 35.8 to 25° favours the force redistribution along the plug but its benefit is outbalanced by the local distribution within the exhaust. As the FPR increases, the benefits offered by a smoother plug arc contribute to beneficial forward forces on the rear-ward facing surfaces whilst maintaining equivalent forces within the exhaust. These observations lead to slender plug-cone shapes preventing sharp accelerations along the plug arc just downstream the exhaust and contributing to large entropy losses.

4.3.3 Overall benefits

In addition to the benefits obtained on the force redistribution along the plug-cone, improved aerodynamic performance arises from the reduction in size of the nacelle length with a smaller wetted surface and a slight reduction in entropy, as observed in Fig. 23. From an energy standpoint, using a compact nacelle for the propulsor over the baseline reduces the overall viscous dissipation rate Φ by 4 and 20% for the larger propulsor throat area, under FPR ratios of 1.20 and 1.50, respectively. These benefits therefore translate to lower fan power demand for the same net axial force, thus power savings, or to a larger force contribution from the thruster relative to the two main engines under the wings.

Table 2. Comparison of fuel saving coefficients (FSC) in percent between the baseline retrofit and the re-scaled turbofans of Concept A: $L_{\text{slope}}/L_{\text{tail}} = 0.5$, $R_{\text{hub}}/R_{\text{fus}} = 0.4$, BLR = 44.0%, and FPR = 1.30, and Concept B: $L_{\text{slope}}/L_{\text{tail}} = 0.6$, $R_{\text{hub}}/R_{\text{fus}} = 0.3$, BLR = 42.8%, and FPR = 1.29, relative to existing projects (with * denoting assumed values)

	Concept A	Concept B	CENTRELINE [8]	STARC-ABL [35]
$x_{\text{fan}}/L_{\text{fus}}$ (-)	0.87	0.90	0.88	0.94*
$R_{\text{hub}}/R_{\text{fus}}$ (-)	0.40	0.30	0.25	0.15*
FPR (-)	1.30	1.29	1.35	1.25
FSC (Retrofit) (%)	10.30	11.10	–	–
FSC (Re-scaled) (%)	15.30	14.04	11.5 [36]	12.8

Nonetheless, these observations are made on a unique propulsor position along the tail and cannot be generalised to all combinations shown in Fig. 17. Whereby possible, the intake length is therefore reduced to favour more compact nacelles, leaving a longer and less steep plug-cone, to offer benefits to the flow redistribution and energy utilisation. An example of optimisation studies on compact exhausts is studied in Ref. [32] whereby improvements of 0.32% of the total aircraft thrust requirement is observed from their reference.

4.4 Auxiliary savings from re-scaled turbofans

A benefit from producing part of the aircraft propulsive force requirement from the thruster is to re-scale the main power-plants under the wings. Maintaining a similar specific thrust, the fan by-pass and pressure ratios can be reduced to generate the output force and feed the aft-mounted fan. To that end, following the work from Giannakakis et al. on the propulsion system characteristics along a typical SMR aircraft mission [33], the baseline turbofans are re-scaled based on the top-of-climb conditions.

To ensure a constant vehicle speed at cruise, state-of-the-art turbofans propelling single-aisle aircraft are used, e.g. CFM LEAP-1 or PW1100G. The two-spool turbofan architecture developed by Zhao and Yao [27] is composed of an 11:1 by-pass ratio single-stage fan, 3-stage intermediate-pressure and 10-stage high-pressure compressor, and 2-stage high-pressure and 7-stage low-pressure turbine for an overall pressure ratio of 44. The free-stream conditions are defined following the International Standard Atmosphere (ISA) model based on the cruise altitude and Mach number and assuming isentropic inflow conditions. The engine performance is evaluated at on-design from which a nacelle drag estimation sub-process determines the nacelle drag based on flight conditions [34] to determine an installed thrust-specific fuel consumption (SFC). Whilst the size and components of the reference aircraft's engines are simply retrofitted in the propulsive fuselage concept, the core is assumed constant and the fan diameter, or by-pass ratio, is scaled down here to provide the adequate force and power required.

Table 2 summarises the fuel savings difference from the retrofit engines and their re-scaled versions for the cruise segment considered herein and the two propulsors down-selected from Fig. 21. It is opined that concept B from Fig. 21(b) has diminishing returns compared to concept A from Fig. 21(a) through the re-scaling of the engine. This is explained as both PFC incorporate the same re-designed turbofans, which is designed to provide the power off-take of concept A, yielding the best benefits. Overall, whilst both propulsors are sensibly similar and only vary by their position, additional savings of between 3 and 5% are obtained with the newly designed turbo-electric architectures, neglecting practical transmission deficiencies and mass changes.

Concept B showcases the best savings when considering retrofit engines under the wings. Its thruster is installed at 90% of the fuselage length, a relative hub radial position of 30% of the fuselage radius and a fan operating at a pressure ratio of 1.29. Comparatively to the existing concepts, the axi-symmetric concept from CENTRELINE installs its thruster at 88% of the fuselage length with a hub positioned at 25% of the fuselage radius and operates at a FPR of 1.35 [8]; and the STARC-ABL with an axi-symmetric fuselage installs its thruster at 94% of its chord, relative hub position of 15% and FPR of

1.25. Despite being designed for long-haul flights with a fuselage length of 67m, the former concept agrees with the non-dimensional parameters of this study whilst the latter, designed for a similar mission features a smaller hub radius enabled by its tapered slope.

5.0 Conclusion

Fundamental design features on a novel propulsive fuselage concept aircraft are presented. The aerodynamic sensitivity to fuselage design changes is assessed by focusing on boundary layer properties and energy recovery potential. First, it is observed that the nose shape has a mere impact on the PER as long as its design impart a shock-free flow behind it. As for the tail designs, slender and complex fuselage tail designs would offer higher energy harvest (+0.8%) whilst morphed tails with thin propulsor hubs improve energy recovery (+0.7%) and performance ensuring the critical inclination angles for propulsor integration are not reached. Maximising this metric becomes instrumental to down-select a tail shape candidate, and can be achieved before the full integration of a BLI propulsor with an aero-propulsive assessment at a lower computational cost.

In the evaluation of PER, the different definitions successively improved are compared. Whilst the former definition from Ref. [22] is incomplete by not accounting for pressure-work effects, the approximation in Ref. [24] that the residual rate of volumetric pressure-work is equivalent to that of the irreversible component is acceptable. This paper shows that only small discrepancies appear in scenarios of strong compression-dilation processes in comparison with the more accurate definition from this work. This is enabled by the incorporation of a velocity field decomposition within a mechanical energy balance.

Through a design exploration of different propulsor locations, sizes and fan pressure ratios, an application of an enhanced energy-based aero-propulsive performance assessment is followed at cruise. The best performance compromise between fuel savings and share of propulsive force between the thruster and the turbofans is generally obtained for propulsors integrated on a low fuselage hub radius, for a fan axial position around the mid-tail, or 90% of the fuselage chord length. These combinations enable greater haverstable energy from the streamlined flow driven by the slope, whilst preventing strong shocks and flow separation along the plug-cone. As regards the propulsor operation, smaller propulsors benefit from the ingestion of the most beneficial part of the boundary layer flow, minimising the installation effects upstream, reducing the power input required from the fan and thus yielding greater savings. It is shown that smaller propulsors slow the flow down further forward up to a fan radius upstream and grow the boundary layer thickness by 4%, whereas larger propulsors thicken the boundary layer by 8% and reduce the flow speed up to two fan radii, specifically in the viscous sub-layer region.

An inverse relationship exists between the force share and the fuel savings. For a given propulsor design, a maximum share of the overall aircraft propulsive force requirement is achievable to maximise fuel savings. However, this can be further enhanced by increasing the compactness of the nacelle and thus slenderness of the plug-cone where a greater output force can be achieved, reducing the propulsive force requirement from the turbofans and enabling a larger down-scaling of them (an additional 5% fuel savings for the cruise segment considered). A downside is the unavoidable rise in the propulsor radial distortion index that requires a higher order propulsion modelling to transport the distortion through the fan stage and ensure its operability.

Acknowledgements. This work was conducted within the SUBLIME (Supporting Understanding of Boundary-Layer Ingestion Model Experiment) project as part of the Clean Sky 2 Joint Undertaking which has received funding from the European Union's Horizon 2020 research and innovation programme under Grant Agreement No. 864803. The authors thank Xin Zhao and Huadong Yao for the development of the turbofans model and the generation of the performance maps, and Panagiotis Giannakakis for the discussions.

Competing interests. The authors declare no competing interests.

Authorship contribution statement. Nicolas G.M. Moirou: Conceptualisation, Data Curation, Investigation, Methodology, Visualisation, Writing – original draft, Writing – review & editing. Ngonidzashe E. Mutangara: Investigation, Visualisation, Writing – original draft. Drewan S. Sanders: Project Administration, Supervision, Validation, Writing – review & editing.

References

- [1] *European Commission Flightpath 2050 Europe's Vision for Aviation, 2011.*
- [2] Epstein, A.H. Aeropropulsion for commercial aviation in the twenty-first century and research directions needed, *AIAA J.*, 2013, **52**, (5), pp 901–911.
- [3] Wislicenus, G.F. Hydrodynamics and propulsion of submerged bodies, *Am. Rocket Soc. J.*, 1960, **30**, (12), pp 1140–1148.
- [4] Sanders, D.S. and Laskaridis, P. Full-aircraft energy-based force decomposition applied to boundary-layer ingestion, *AIAA Journal*, 2020, **58**, (10), pp 4357–4373.
- [5] Moirou, N.G.M., Sanders, D.S. and Laskaridis, P. Advancements and prospects of boundary layer ingestion propulsion concepts, *Progress in Aerospace Sciences*, 2023, **138**, p 100897.
- [6] Battiston, A., Ponza, R. and Benini, E. Design exploration for an axisymmetric rear BLI propulsor, *AIAA Propulsion and Energy 2021 Forum, Virtual Event, AIAA 2021-3470*, 2021.
- [7] Gray, J.S., Mader, C.A., Kenway, G.K.W. and Martins, J.R.R.A. Modeling boundary layer ingestion using a coupled aeropropulsive analysis, *J. Aircraft*, 2018, **55**, (3), pp 1191–1199.
- [8] Habermann, A.L., Zahn, R., Seitz, A. and Hornung, M. Multidimensional parametric study of a propulsive fuselage concept using OpenFOAM, *AIAA Aviation 2020 Forum, Virtual Event. AIAA 2020-2754*, 2020.
- [9] Arntz, A., Atinault, O. and Merlen, A. Exergy-based formulation for aircraft aeropropulsive performance assessment: theoretical development, *AIAA J.*, 2015, **53**, (6), pp 1627–1639.
- [10] Drela, M. Power balance in aerodynamic flows, *AIAA J.*, 2009, **47**, (7), pp 1761–1771.
- [11] Ahuja, J. and Mavris, D.N. Sensitivity of boundary layer ingestion effects to tube and wing airframe design features, *AIAA SciTech 2020 Forum, Orlando, FL, USA. AIAA 2020-1523*, 2020.
- [12] Moirou, N.G.M. Aero-propulsive Performance Assessment Approach to Boundary Layer Ingestion Aircraft, PhD thesis, Cranfield University, Cranfield, UK, 2023.
- [13] Drela, M. Development of the D8 transport configuration, 29th AIAA Applied Aerodynamics Conference, Honolulu, HI, USA. AIAA 2011-3970, 2011.
- [14] Wiart, L., Atinault, O., Paluch, B., Hue, D. and Grenon, R. Development of NOVA aircraft configurations for large engine integration studies, 33rd AIAA Applied Aerodynamics Conference, Dallas, TX, USA, AIAA 2015-2254, 2015.
- [15] Kenway, G.K. and Kiris, C. Aerodynamic shape optimization of the STARC-ABL concept for minimal inlet distortion, *AIAA/ASCE/AHS/ASC Structures, Structural Dynamics, and Materials Conference*, 2018, Kissimmee, FL, USA, AIAA 2018-1912, 2018.
- [16] Lamprakis, I., Sanders, D.S. and Laskaridis, P. Energy-based aerodynamic loss and recovery characteristics of adiabatic and heated fuselages, *J. Aircraft*, 2023a, **60**, (6), pp 1947–1964.
- [17] Mutangara, N.E., Sanders, D.S., Laskaridis, P., Hart, P.L. and Schmitz, S. A unified partial pressure field and velocity decomposition approach toward improved energetic aerodynamic force decompositions, 57th 3AF International Conference on Applied Aerodynamics, Bordeaux, France, 2023.
- [18] ANSYS Inc. *Ansys® ICFM CFD Release 20.2*, 2020b.
- [19] Celik, I.B., Ghia, U., Roache, P.J., Freitas, C.J., Coleman, H. and Raad, P.E. Procedure for estimation and reporting of uncertainty due to discretization in CFD applications, *J. Fluids Eng.*, 2008, **130**, (7), p 078001.
- [20] ANSYS Inc. *Ansys® Fluent Release 20.2*, 2020a.
- [21] Drela, M. Boundary layer analysis, *Flight Vehicle Aerodynamics*, Chapter 4. MIT Press, 2014, Cambridge, Massachusetts, pp 57–98.
- [22] Sanders, D.S. Boundary Layer Ingestion Performance Assessments with Application to Business Jets, PhD thesis, Cranfield University, Cranfield, UK, 2018.
- [23] Aguirre, M.A., Duplaa, S., Carboneau, X. and Turnbull, A. Velocity decomposition method for exergy-based drag prediction, *AIAA J.*, 2020, **58**, (11), pp 4686–4701.
- [24] Lamprakis, I., Sanders, D.S. and Laskaridis, P. Fundamental concepts of boundary layer ingestion propulsion, *J. Aircraft (Submitted)*, 2023b.
- [25] Bell, J.H. and Mehta, R.D. Contraction Design for Small Low-Speed Wind Tunnels. Technical Report CR-177488, Stanford University, 1988.
- [26] Langley, M.J. The Design of Axisymmetric Cowls for Padded Nacelles for High By-Pass Ratio Turbofan Engines. Technical Report R&M 3846, Aircraft Research Association Limited, Bedford, UK, 1979.
- [27] Zhao, X. and Yao, H. BLI turbofan performance maps, Technical Report RP0019, Chalmers University of Technology, Gothenburg, Sweden, 2022.
- [28] Zachos, P.K., Frascella, M., MacManus, D.G. and Gil-Prieto, D. Pressure Flowfield and Inlet Flow Distortion Metrics Reconstruction from Velocity Data, 2017, **55**, (9), pp 2929–2941.
- [29] Malsaac, B. and Roy, L. *New and Future Gas Turbine Propulsion System Technologies*, chapter 11, John Wiley & Sons, 2011, pp 257–278.
- [30] Peters, A., Spakovszky, Z.S., Lord, W.K. and Rose, B. Ultrashort nacelles for low fan pressure ratio propulsors, *J. Turbomach.*, 2014, **137**, (2), p 021001.
- [31] Castillo Pardo, A. and Hall, C.A. Effects of sideslip direction on a rear fuselage boundary layer ingesting fan, *J. Turbomach.*, 2022, **144**, (12), p 121012.
- [32] Matesanz-García, J., Piovesan, T. and MacManus, D.G. Aerodynamic optimization of the exhaust system of an aft-mounted boundary layer ingestion propulsor, *Int. J. Numer. Methods Heat Fluid Flow*, 2022, **33**, (4), pp 1295–1318.

- [33] Giannakakis, P., Maldonado, Y.-B., Tantot, N., Frantz, C. and Belleville, M. Fuel burn evaluation of a turbo-electric propulsive fuselage aircraft, AIAA Propulsion and Energy 2019 Forum, Indianapolis, IN, USA. AIAA 2019-4181, 2019.
- [34] Heidebrecht, A. and MacManus, D.G. Surrogate model of complex non-linear data for preliminary nacelle design, *Aerospace Sci. Technol.*, 2019, **84**, pp 399–411.
- [35] Yildirim, A., Gray, J.S., Mader, C.A. and Martins, J.R.R.A. Boundary-layer ingestion benefit for the STARC-ABL concept, *J. Aircraft*, 2022, **59**, (4), pp 896–911.
- [36] Seitz, A., Habermann, A.L. and van Sluis, M. Optimality considerations for propulsive fuselage power savings, *J. Aerospace Eng.*, 2020, **235**, (1), pp 22–39.